University of Groningen

Anisotropic conductance at improper ferroelectric domain walls

Meier, D.; Seidel, J.; Cano, A.; Delaney, K.; Kumagai, Y.; Mostovoy, M.; Spaldin, N. A.; Ramesh, R.; Fiebig, M.

IMPORTANT NOTE: You are advised to consult the publisher's version (publisher's PDF) if you wish to cite from it. Please check the document version below.

Document Version
Publisher's PDF, also known as Version of record

Publication date:
2012

Link to publication in University of Groningen/UMCG research database

Supplementary Information

Anisotropic conductance at improper ferroelectric domain walls

D. Meier[1,2,*], J. Seidel[1,3,*], A. Cano[4], K. Delaney[5], Y. Kumagai[6], M. Mostovoy[7], N. A. Spaldin[6], R. Ramesh[1,2,3] & M. Fiebig[8]

[1]Department of Physics, University of California, Berkeley, California 94720, USA

[2]Department of Materials Science and Engineering, University of California, Berkeley, California 94720, USA

[3]Materials Sciences Division, Lawrence Berkeley National Laboratory, California 94720, USA

[4]European Synchrotron Radiation Facility, 6 Rue Jules Horowitz, 38043 Grenoble, France

[5]Materials Research Laboratory, University of California, Santa Barbara, California 93106, USA

[6]Department of Materials, ETH Zürich, Wolfgang-Pauli-Strasse, 8093 Zürich, Switzerland

[7]Zernike Institute for Advanced Materials, University of Groningen, Nijenborgh 4, 9747 AG Groningen, The Netherlands

*These authors contributed equally to this work

1. Local *I-V* measurements with negative and positive bias voltage

Figure S1a shows a schematic of the experimental setup. All measurements were performed under ambient conditions using n-doped conductive diamond tips. The network of domains in $ErMnO_3$ prohibits a straight conductance path through the crystal (thickness ~200 microns). Nevertheless, variations in the local conductance allow us to image the distribution of ferroelectric domains and domain walls at the surface. The electrical circuit from the c-AFM tip to the bottom electrode is in any case closed because of the finite conductance of the sample.

The local *I-V* curves obtained on the *x*-oriented sample in the centre of a ferroelectric domain and at domain walls exhibiting head-to-head and tail-to-tail configurations are displayed in Fig. S1b. For negative bias voltages the electronic conductance of tail-to-tail (head-to-head) domain walls appears to be enhanced (suppressed) with respect to the centre of the domain. In contrast, both types of domain wall show equivalent conductance properties for positive bias voltages, at which they are slightly less conductive than the ferroelectric domains. The locally obtained nonlinear *I-V* curves are in good agreement with *I-V* curves extracted from the spatially resolved measurements in Fig. 2c in the main text and indicate the presence of a
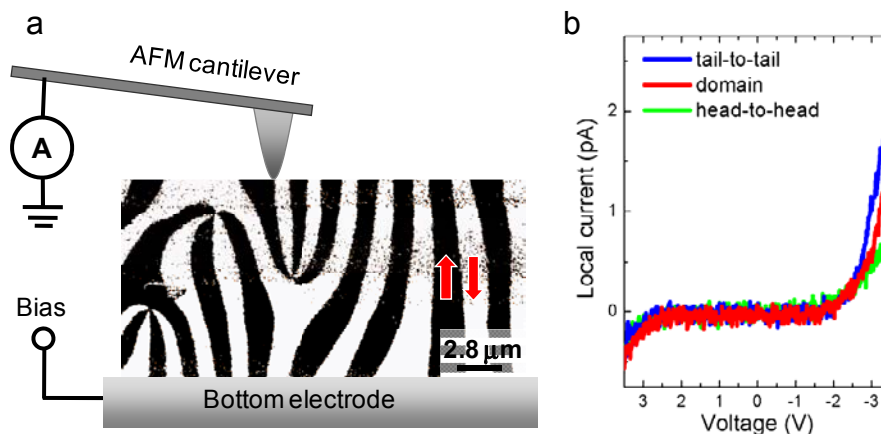
Figure S1. **Schematic setup and local *I-V* curves. a** Setup for c-AFM measurements. **b** Local *I-V* characteristics of head-to-head and tail-to-tail domain walls and in the centre of a domain in $ErMnO_3$.

Schottky-like barrier at the sample-tip interface. In consequence, contrasts are observable in our c-AFM measurements for negative bias.

2. Angular dependence of the conductance and width of the domain wall

The angular dependence of the normalized local current and the domain wall width shown in Figs. 2d and 2e of the main text were determined as detailed in the following.

Figures S2a and S2b display examples for a "domain wall loop" covering all the angles between 0° and 360°. The positions of the maximum and minimum of the measured currents are marked in Fig. S2a. These extrema correspond, respectively, to the tail-to-tail and head-to-head polarisation configurations at the wall.

The definition of the wall orientation angle α is presented in Fig. S2c. It is defined as the angle between the z-axis and the normal of the ellipse tangent at the position where the conductance is measured. Note that two cases have to be distinguished: One in which the polarisation along the inside contour of the ellipse is parallel to the z-axis and one in which it is antiparallel to the z-axis. The two examples in Figs. S2a and S2b both correspond to the parallel case. For an antiparallel alignment a phase shift of 180° has to be considered to sustain a unique relation between the angle α and the type of domain wall (head-to-head wall: $\alpha = 0°$; tail-to-tail wall: $\alpha = 180°$).

This leads to the angular dependence shown in Fig. S2d. Here, normalized c-AFM currents defined as $(I_{wall}(\alpha) - I_{bulk})/I_{bulk}$ are plotted with I_{bulk} being the bulk background current as averaged from the images. $(I_{wall}(\alpha) - I_{bulk})/I_{bulk}$ is referred to as normalized domain wall current and is used as a measure of the normalized conductance $G^{norm}(\alpha)$. Figure S2d shows
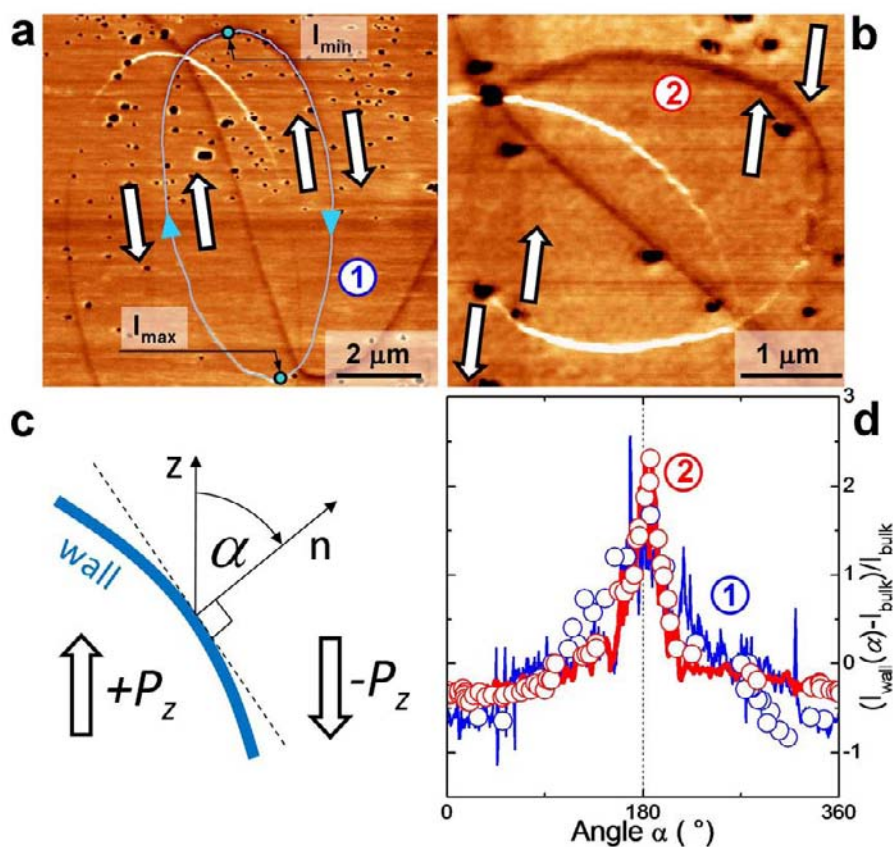
Figure S2. **Angular dependence of domain wall conductance. a** The blue line shows the pathway along which the local conductance has been extracted from the c-AFM image. Maximum and minimum of the observed current are indicated. White arrows denote local polarisation directions of the domains adjacent to the considered "domain wall loop". **b** Another domain wall loop for comparison with panel a. **c** Definition of the domain wall orientation angle. **d** Plots of the normalized angular conductance extracted from Figs. S2a and S2b.

that similar results are obtained on the loops in Figs. S2a and S2b. The solid lines (red and blue) in Fig. S2d represent the normalized current values observed along closed loops as depicted in Fig. S2a. In contrast, the data points (blue and red circles) are extracted from cross sections perpendicular to the wall. For this purpose a Gaussian profile was fitted to the domain wall cross section so that its maximum can be assigned as the local current and the full width at half maximum as the local domain wall width. Note that consistent results are obtained with the two methods. A common feature of all data sets is a small shift away from

90° and 270° (side-by-side wall configuration) regarding the zero-crossing of $(I_{wall}(\alpha)$ $- I_{bulk})/I_{bulk}$. This shift can be attributed to local defects (like the black spots in Figs. S2a and S2b), the unknown progression of the domain walls into the sample, and the proximity of a domain wall intersection. The influence of the latter can be seen by comparing the peak positions of the normalized current for the "domain wall loops" in Figs. S2a and S2b.

3. DFT calculation details

Density functional calculations were performed using the VASP code [G. Kresse and J. Furthmüller, *Phys. Rev. B* **54**, 11169 (1996)] with the GGA+U method in the Dudarev implementation [J. P. Perdew, K. Burke, and M. Ernzerhof, *Phys. Rev. Lett.* **78**, 1396 (1997); S. L. Dudarev et al., *Phys. Rev. B* 57, 1505 (1998)] and a U_{eff} of 5 eV. PAW potentials with semi-core states in the valence (Y: (4s)2(4p)6(4d)1(5s)2, Mn: (3d)5(4s)2, O: (2s)2(2p)4) were used. Convergence parameters were an energy cutoff 550 eV, SCF energy convergence 10^{-5} eV, and a Gamma-centered 6×6×1 k-point grid. We imposed an antiferromagnetic magnetic configuration with alternating ferrimagnetic layers (up-up-down, down-down-up, etc.). With these parameters the band gap of ideal bulk $YMnO_3$ at the experimental lattice parameters and ionic positions is 1.35 eV.
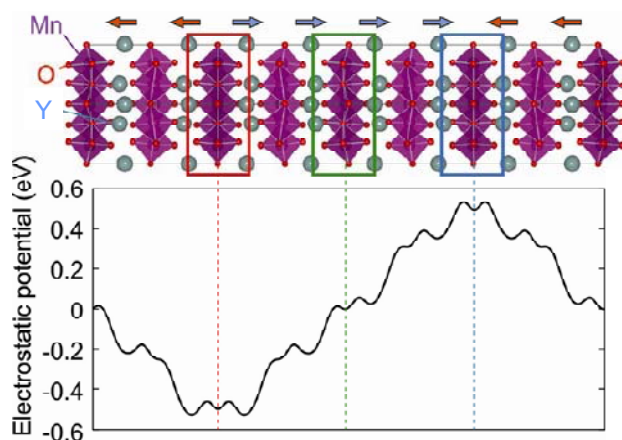
Figure S3. **Calculated electrostatic potential at tail-to-tail (red) and head-to-head (blue) domain walls.** Note the change in slope of the potential at the walls and its change in sign in the mid-domain region (green).

To model the head-to-head and tail-to-tail domain walls, we constructed a supercell containing four layers of up-polarised $YMnO_3$ at the experimental positions of the ferroelectric structure [Gibbs *et al.*, *Phys. Rev. B* **83**, 094111 (2011)] alternating with four layers of down-polarised along the z direction. The positions of the oxygen and manganese

ions in the domain walls were set to the paraelectric values and mirror symmetry was imposed. The resulting unit cell, with 120 atoms, contained one head-to-head and one tail-to-tail domain wall. The ions were fixed at these positions and not allowed to relax. With this configuration the variation in electrostatic potential (Figure S3) across the cell was found to be ~1 eV; in supercells with fewer polar layers and/or reduced magnitudes of the polarisation we obtained a correspondingly smaller variation in the electrostatic potential. The shifts in the band edges shown in Fig. 3d of the main paper are in concordance with the calculated variation in electrostatic potential.

To test the robustness of our conclusions, we repeated our calculations using the ABINIT code [X. Gonze et al., *Comput. Mater. Sci.* **25**, 478 (2002)] and a smaller (1/3 the size) in-plane unit cell which neglected the tiltings of the MnO_5 polyhedra. While this structure and code resulted in a smaller band gap, our results yielded qualitatively the same physical picture.

4. Charge redistributions and surface conductivity

In this section we describe the detailed derivation of the theoretical conductance and wall width depicted in Fig. 3. The distribution of the current injected by the c-AFM tip into the sample can be obtained from the equation of continuity $\nabla \cdot j = 0$ under the boundary conditions imposed by the tip. We follow a perturbative approach, in which the current density is given by $j = -\sigma \nabla \delta\phi$, where σ is the sample conductivity in absence of bias (determined by the equilibrium distribution of charge carriers) and $\delta\phi$ is the change of electric potential due to the bias voltage.

In our measurements, we are dealing with interfaces in which there is a redistribution of mobile charge carriers due to the bound charges that accompany the abrupt (longitudinal) variations of the electric polarization from $+P_z$ to $-P_z$. When the c-AFM scans are performed on a z-oriented crystal, this redistribution takes place across the entire xy-surface of the sample. On the other hand, when the yz-plane is scanned, such redistribution occurs in the vicinity of the domain walls only.

4.1. Crystals oriented perpendicular to z

For scans of z-oriented crystals, for example, the conductivity of the sample can be approximated by

$$\sigma = \begin{cases} \sigma_{surf} & -d < z < 0 \\ \sigma_{bulk} & z < -d \end{cases} \quad \text{(S1)}$$

where σ_{bulk} is the bulk conductivity of the system and σ_{surf} is the average conductivity at the surface obtained from the corresponding accumulation/depletion of charge carriers over the distance d.
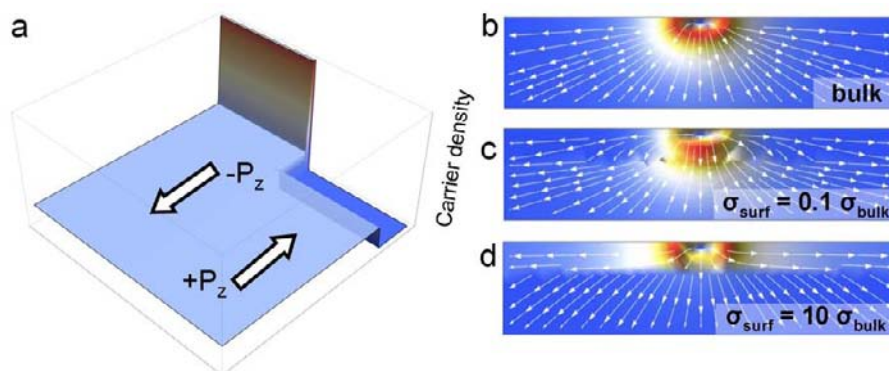
Figure S4. **Calculated surface charge carrier density and related current distribution. a** Landscape of conductivity on the surface of a z-oriented sample. Mobile charge carriers (holes) accumulate on the $-P_z$ domains to screen the bound charges at the surface leading to enhanced conductivity. In contrast, a depletion occurs at the surface of the $+P_z$ domains so that the conductivity is reduced compared to the bulk. **b, c, d** Distribution of the current injected by the c-AFM tip for the bulk, $+P_z$ domains, and $-P_z$ domains, respectively (see text for details).

Both σ_{surf} and d obviously depend on the bound charges that appear at the surface (that is, on the spontaneous polarization P_z). In this model, the potential $\delta\phi$ and the corresponding distribution of current injected by the c-AFM tip can be obtained analytically using the image charge method:

$$\delta\phi(x,y,z) = \begin{cases} \dfrac{I}{2\pi\sigma_{surf}} \displaystyle\sum_{n=-\infty}^{\infty} \dfrac{f^{|n|}}{\sqrt{\rho^2 + (z-2nd)^2}} & -d < z < 0 \\[3ex] \dfrac{I}{2\pi\sigma_{bulk}} \displaystyle\sum_{n=0}^{\infty} \dfrac{gf^n}{\sqrt{\rho^2 + (z-2nd)^2}} & z < -d \end{cases} \quad (S2)$$

Where $\rho^2 = x^2 + y^2$, $f = (\sigma_{surf} - \sigma_{bulk})/(\sigma_{surf} + \sigma_{bulk})$, and $g = 2\sigma_{surf}/(\sigma_{surf} + \sigma_{bulk})$. This potential corresponds to the injection of current by a point source placed at the surface of the sample (at the position $x = y = 0$). The c-AFM tip can be seen as a distribution of such point sources over the surface of the sample and, accordingly, the resulting potential and distribution of current can be obtained as an integral over these sources.

Our results are summarized in Fig. S4 and lead to the following explanation for the domain wall width observed in scans on the z-oriented sample as shown in Figs. 1a, b, and c.

Since the system is a p-type semiconductor, itinerant charge carriers (holes) are expected to accumulate at the surface of the $-P_z$ domains while they will deplete at the surface of the $+P_z$ domains. Thus, the carrier density changes from accumulation to depletion across the domain wall giving rise to the nontrivial landscape of conductivity shown in Fig. S4a. Such a landscape, however, does not suffice to explain the width of the electrically dressed walls

since the change from accumulation to depletion takes place within a distance in the order of the Debye length which can be estimated as 2 nm in our system.

The key ingredient is the distribution of current injected by the c-AFM tip. The distribution is such that, when the conductivity at the surface is lower than underneath in the bulk, the region that is actually probed by the c-AFM tip is similar (or smaller) in size than the tip itself. This is shown in Figs. S4b and S4c. This region, however, undergoes a sizeable broadening whenever the conductivity at the surface increases due to the corresponding accumulation of charges (see Fig. S4d). This convolution between tip and domain-wall properties results in the bias-dependent broadening of the electrically dressed domain walls documented in Fig. 1 of the main text.

4.2. Crystals oriented parallel to z

The aforementioned solution can be straightforwardly generalized to account for the redistribution of charges probed by the c-AFM tip when the yz-plane is scanned. We assume that the sample occupies the $y < 0$ region. Then, the landscape of conductivity associated with the domain wall can be taken as

$$\sigma = \begin{cases} \sigma_{DW} & -d < z < d \\ \sigma_{bulk} & otherwise \end{cases} \quad (S3)$$

where σ_{DW} represents the conductivity of the domain wall, as described in the main text, while the effective width $w = 2d$ is found by requiring that the total number of screening charges for the model Eq. S3 equals the bound charge at the domain wall:

$$d = \frac{\int_0^\infty dx \left(1 - \exp(-\frac{\phi(x)}{k_B T})\right)}{1 - \exp(-\frac{\phi_{DW}}{k_B T})} = \frac{\varepsilon}{ep_0} \frac{\int_0^\infty dx \phi''(x)}{1 - \exp(-\frac{\phi_{DW}}{k_B T})} = \frac{\sqrt{\frac{\varepsilon k_B T}{e^2 p_0}} \Pi \cos\alpha}{1 - \exp(-\frac{\phi_{DW}}{k_B T})} \quad (S4)$$

The distribution of current injected by the c-AFM tip can then be obtained from the potential

$$\delta\phi(x,y,z) = \begin{cases} \dfrac{I}{2\pi\sigma_{bulk}} \sum_{n=0}^{-\infty} \dfrac{gf^n}{\sqrt{\rho^2 + (z - 2nd)^2}} & d < z \\ \dfrac{I}{2\pi\sigma_{DW}} \sum_{n=-\infty}^{\infty} \dfrac{f^{|n|}}{\sqrt{\rho^2 + (z - 2nd)^2}} & -d < z < d \\ \dfrac{I}{2\pi\sigma_{bulk}} \sum_{n=0}^{\infty} \dfrac{gf^n}{\sqrt{\rho^2 + (z - 2nd)^2}} & z < -d \end{cases} \quad (S5)$$

For a tip placed on top of the domain wall (say at $x = y = z = 0$) whose effective radius r is much smaller than d, the conductance is then

$$G \sim \frac{\sigma_{DW}}{1 + \frac{r}{d} \ln \frac{\sigma_{DW} + \sigma_{bulk}}{2\sigma_{bulk}}}. \quad (S6)$$

Using Eq. (S5) this expression is obtained from the ratio between the total current injected by the tip, I, and the electric potential at the tip:

$$V \approx \frac{I}{2\pi\sigma_{DW}} \left(\frac{1}{r} + \frac{1}{d} \sum_{n=1}^{\infty} \frac{f^n}{n} \right) = \frac{I}{2\pi\sigma_{DW}r} \left(1 + \frac{r}{d} \ln \frac{1}{1-f} \right) \quad (S7)$$

In this way, we account for the nontrivial spreading of current out of the domain walls as illustrated in Figs. 3c and 3d of the main text. Note that this spreading also affects the angular dependence of the domain wall conductance as indicated by the corresponding fit shown in Fig. 3a of the main text.